

Trapped orbits and solar-neighbourhood kinematics

James Binney^{1*}

¹*Rudolf Peierls Centre for Theoretical Physics, Clarendon Laboratory, Parks Road, Oxford, OX1 3PU, UK*

19 February 2024

ABSTRACT

Torus mapping yields constants of motion for stars trapped at a resonance. Each such constant of motion yields a system of contours in velocity space at the Sun and neighbouring points. If Jeans’ theorem applied to resonantly trapped orbits, the density of stars in velocity space would be equal at all intersections of any two contours. A quantitative measure of the violation of this principal is defined and used to assess various pattern speeds for a model of the bar recently fitted to observations of interstellar gas. Trapping at corotation of a bar with pattern speed in the range $33 - 36 \text{ Gyr}^{-1}$ is favoured and trapping at the outer Lindblad resonance is disfavoured. As one moves around the Sun the structure of velocity space varies quite rapidly, both as regards the observed star density and the zones of trapped orbits. The data seem consistent with trapping at corotation.

Key words: Galaxy: kinematics and dynamics – galaxies: kinematics and dynamics – methods: numerical

1 INTRODUCTION

The release of kinematic data from Gaia in 2018 April allowed the study of velocity space with unprecedented precision. Study of this space was opened up by the first astrometric satellite, Hipparcos (Perryman et al. 1997). Hipparcos did not provide line-of-sight velocities so Dehnen (1998) mapped velocity space using 5-dimensional data. The all-sky nature of the Hipparcos catalogue enabled him to infer the probability density of stars in velocity space, but individual stars could only be assigned locations in velocity space on the release of data from the Geneva-Copenhagen Survey (Nordström et al. 2004; Holmberg et al. 2009; Casagrande et al. 2011, hereafter GCS), which measured, inter alia, line-of-sight velocities v_{\parallel} . Once the GCS data were available it became clear that little of the structure in velocity space is due to dissolving groups of coeval stars since prominent structures contained stars widely spread in age and chemical composition (Famaey et al. 2005).

Dehnen (1999, 2000) proposed that the ‘Hercules stream’, the dominant feature at low azimuthal velocity V , is caused by the outer Lindblad resonance (OLR) of the Galactic bar. More recently Pérez-Villegas et al. (2017) have attributed the Hercules stream to the bar’s corotation resonance, but this association is controversial (Monari et al. 2017; Trick et al. 2019; Fragkoudi et al. 2019). De Simone et al. (2004) investigated the possibility that much of the remaining structure is caused by spiral arms, a possibility

that was been examined several times subsequently (e.g., Sellwood 2010; Hahn et al. 2011; McMillan 2011, 2013).

The last decade has seen growing awareness of the value of angle-action coordinates for Galactic dynamics, in part due to the discovery of an algorithm, the ‘Stäckel Fudge’ (Binney 2012), for computing angles and actions (θ, \mathbf{J}) from ordinary phase-space coordinates (\mathbf{x}, \mathbf{v}) of particles moving in any realistic axisymmetric Galactic potential $\Phi(R, z)$. Several papers (e.g. Binney & Schönrich 2018; Bland-Hawthorn et al. 2019; Trick et al. 2019; Vasiliev 2019; Hunt et al. 2019) have used this algorithm to discuss distributions of angle-action coordinates using data from Gaia’s second data release (Gaia Collaboration & Katz 2018).

The distribution of stars in three-dimensional action space has attracted the most attention because, by the theorem of Jeans (1916), a relaxed Galaxy would be fully described by this distribution. Moreover, each point in this space is associated with three characteristic frequencies Ω_r , Ω_{ϕ} and Ω_z , and the planes on which these frequencies satisfy a resonant condition $\mathbf{N} \cdot \boldsymbol{\Omega} = m\Omega_p$ are of interest. Here \mathbf{N} is a vector with integer components, m is another integer and Ω_p is the ‘pattern speed’ of the Galactic bar or a system of spiral arms. Several attempts have been made, with mixed success, to identify features in the computed density of stars in action space with such resonant planes (Monari et al. 2017, 2019; Fragkoudi et al. 2019; Hunt et al. 2019).

Any system of angle-action coordinates is a valid system of canonical coordinates for phase space and the distribution of stars in its action space may be of interest, but the system is most valuable if the Galaxy’s Hamiltonian $H(\mathbf{x}, \mathbf{v})$ is a function $H(\mathbf{J})$ of the actions alone. Hitherto stars have been

* E-mail: binney@physics.ox.ac.uk

assigned locations in action space under the assumption that the Galaxy’s gravitational field is axisymmetric although the bar and spiral structure ensure that it is not. Hence the coordinates employed do not make the true Hamiltonian a function $H(\mathbf{J})$. In this paper the mapping between velocity space and action space is discussed using actions that make the Hamiltonian of a realistic model of the Galaxy’s barred gravitational field a function $H(\mathbf{J})$ of the actions only.

Introduction of a rotating bar qualitatively changes the structure of action space. In fact, through the phenomenon of resonant trapping, it splits action space into disjoint pieces because there is a separate action space for each family of trapped orbits. Previous papers in this series Binney (2016, 2018) demonstrated that torus mapping (Binney & McMillan 2016, and references therein) in combination with resonant perturbation theory, enables one to compute, with remarkable accuracy, the mapping $(\boldsymbol{\theta}, \mathbf{J}) \rightarrow (\mathbf{x}, \mathbf{v})$ for any family of resonantly trapped orbits. One can also compute the boundaries of the region in the action-space of the underlying axisymmetric model that should be excised and replaced with the action space of the trapped orbits. Outside this excised area non-resonant perturbation theory can be used to modify actions computed under the assumption of axisymmetry into actions that reflect the presence of the bar.

Section 2 reviews the methodology by which maps $(\boldsymbol{\theta}, \mathbf{J}) \rightarrow (\mathbf{x}, \mathbf{v})$ are computed for resonantly trapped orbits. Section 3 discusses the structure in velocity space of orbits trapped at corotation, while Section 4 presents a similar exercise for orbits trapped at the OLR. Section 5 compares predictions for trapping at corotation with Gaia data for velocity spaces at points a kpc distant from the Sun. Section 6 sums up.

2 BACKGROUND

The work reported here relies on torus mapping, which was introduced by McGill & Binney (1990), completed by Binney & Kumar (1993) and brought to a high state of development in the PhD thesis of Kaasalainen (Kaasalainen 1994, 1995a,b; Kaasalainen & Binney 1994). A publicly available implementation of the technique in C++ was released as the ‘Torus Mapper’ (hereafter TM) by Binney & McMillan (2016). The key idea is that orbital tori in phase space (surfaces $\mathbf{J} = \text{constant}$) can be constructed by injecting an analytically obtained ‘toy torus’ into the Galaxy’s phase space with a canonical map that is adjusted to minimise the variance of the Galaxy’s Hamiltonian within the three-dimensional volume of the injected torus. The toy torus is obtained by solving the Hamilton-Jacobi equation by separation of variables, typically under the assumption of a spherical potential.

The injected torus is characterised by the numbers that define the toy torus and the canonical transformation. Fewer than 100 numbers almost always suffice. Once a torus has been constructed, not only can the position of a star with the given actions be predicted at negligible cost arbitrarily far in the past or the future, but one can determine whether a star will reach any give location \mathbf{x} , and, if it does, determine the velocities it will then have, and the contribution it will make to the stellar density at \mathbf{x} . Consequently, a torus

contains much more information than the time series one obtains by integrating an orbit with a Runge-Kutta or similar algorithm.

Given a grid of injected tori in action space, intervening tori can be quickly constructed by interpolation (Binney & McMillan 2016). This possibility plays a key role in the construction of the tori of trapped orbits by resonant perturbation theory. This theory uses a canonical transformation to isolate a ‘slow angle’ and its conjugate action. One neglects the dependence of the Hamiltonian on the remaining ‘fast’ angles and solves for the motion in the two-dimensional space of the slow angle and action. Traditionally this is done using a pendulum equation. A companion paper Binney (2020) explains why this approach breaks down in the case of Lindblad resonances but can be fixed up within the context of TM.

Resonant perturbation theory works exceptionally well in combination with torus mapping for two reasons. First, torus mapping (which is not a perturbative technique) enables one to construct an integrable Hamiltonian $H_0(\mathbf{J})$ that is much closer to the true Hamiltonian $H(\boldsymbol{\theta}, \mathbf{J})$ than one can come in traditional applications of perturbation theory. Second, TM allows one not only to handle motion in the plane of the slow angle and action more completely than hitherto, but also to include subsequently contributions from the fast angles.

When an orbit becomes trapped, the actions conjugate to its two fast angles remain (approximately) constants of motion, while the slow action can no longer serve as a conserved quantity. Its place as an action is taken by the action of libration \mathcal{J} which is the amplitude of motion in the plane of the slow angle and its action. The variable conjugate to \mathcal{J} is the angle of libration θ_ℓ , which evolves linearly in time with a new angular frequency Ω_ℓ . There is an upper limit \mathcal{J}_{\max} on the action of libration, and Ω_ℓ tends to zero as \mathcal{J} tends to \mathcal{J}_{\max} .

Details of how resonant perturbation theory works and is implemented in the context of TM can be found in Binney (2016, 2018) and a companion paper Binney (2020), which resolves a technical problem that emerged in the course of this study. Here the focus is on comparing the map of local velocity space that emerged from the RVS subset (Gaia Collaboration & Katz 2018) of the Gaia DR2 release (Gaia Collaboration & Brown 2018) with model maps computed by instances of the classes `resTorus_c` and `resTorus_L` that were documented in Binney (2018) and Binney (2020) and can be downloaded with TM. The method `containsPoint` within both these classes returns the number of velocities at which a torus reaches a given point \mathbf{x} together with the values of $\boldsymbol{\theta}$ associated with those visits and the Jacobian determinant

$$D \equiv \left(\frac{\partial(\mathbf{J})}{\partial(\mathbf{v})} \right)_{\mathbf{x}} = \left(\frac{\partial(\mathbf{x})}{\partial(\boldsymbol{\theta})} \right)_{\mathbf{J}} \quad (1)$$

that determines how much the orbit contributes to the stellar density at \mathbf{x} .

2.1 Solar position and velocity

Distances are taken from Schönrich et al. (2019), who adopt 8.27 kpc as the distance to the Galactic centre and $(U_0, V_0, W_0) = (11.1, 250, 7.47) \text{ km s}^{-1}$ as the Sun’s Galac-

tocentric velocity. According to this assumption, the Sun is moving towards the Galactic centre, ahead of the local circular speed $\Theta_0 = 239 \text{ km s}^{-1}$ and up out of the plane.

2.2 Units

The units of mass, length and time are $1 M_\odot$, 1 kpc and 1 Myr . the unit of velocity is then $\text{kpc Myr}^{-1} \simeq 978 \text{ km s}^{-1}$. Actions have units of $\text{kpc}^2 \text{ Myr}^{-1}$. Frequencies are plotted in units of $\text{Gyr}^{-1} = 0.978 \text{ km s}^{-1} \text{ kpc}^{-1}$.

2.3 Galactic potential

The Galactic potential is modelled as the sum of an axisymmetric part and a modulation in azimuthal angle ϕ that carries no net mass. The axisymmetric component is the potential fitted by McMillan (2017) to a variety of data tweaked to yield $R_0 = 8.27 \text{ kpc}$ and $\Theta_0 = 239 \text{ km s}^{-1}$ by increasing the central surface density and scale length of the stellar disc from 8.96×10^8 to $9.2 \times 10^8 M_\odot \text{ kpc}^{-2}$ and from 2.5 to 2.6 kpc .

The bar's contribution to the potential is that fitted by Sormani et al. (2015) to the flow of gas through the disc as mirrored in longitude-velocity plots of HI and CO. The bar's density distribution is

$$\rho_2(r, \vartheta, \phi) = \frac{A}{4\pi G} \left(\frac{v_0 e}{r_q} \right)^2 e^{-2r/r_q} \sin^2 \vartheta \cos(2\phi), \quad (2)$$

where A is the dimensionless strength of the bar, r_q is its scale length and (r, ϑ, ϕ) are spherical polar coordinates. The bar's potential is (Sormani private communication)

$$\Phi_2(r, \vartheta, \phi) = \left(\frac{e^{-2x}(2x^4 + 4x^3 + 6x^2 + 6x + 3) - 3}{20x^3} - \frac{x^2}{5} E_1(2x) \right) A (v_0 e)^2 \sin^2 \vartheta \cos(2\phi), \quad (3)$$

where $x \equiv r/r_q$ and $E_1(x) = \int_1^\infty dt e^{-xt}/t$.

The azimuthal angle is measured relative to the bar's long axis, which rotates at angular frequency Ω_p . Sormani et al. (2015) adopted $v_0 = 220 \text{ km s}^{-1}$, and inferred from longitude velocity plots of HI and CO that with $A \gtrsim 0.4$ and $r_q \simeq 1.7 \text{ kpc}$. the results below are for $A = 0.4$ and $r_q = 1.7 \text{ kpc}$.

3 ORBITS TRAPPED AT COROTATION

At corotation J_ϕ is the slow action that is replaced by \mathcal{J} , and its conjugate angle θ_ϕ is replaced by the angle of libration θ_ℓ . J_r plays the role of the surviving fast action J'_3 .

Fig. 1 shows the location in local velocity space of orbits trapped by the Sormani et al. bar if $\Omega_p = 33 \text{ Gyr}^{-1}$. These orbits were obtained by sampling the action-space plane $J_z = 0.0025 \text{ kpc}^2 \text{ Myr}^{-1}$ on a non-uniform rectangular grid. The chosen value of J_z causes stars to make excursions $\sim 300 \text{ pc}$ above and below the plane, but plays no essential role; any similar choice would yield equivalent results. We restrict attention to instants when a star passes the Sun moving upwards.

The J_r coordinates of the grid points were uniformly spaced in $\sqrt{J_r}$, a choice which yields velocities which lie

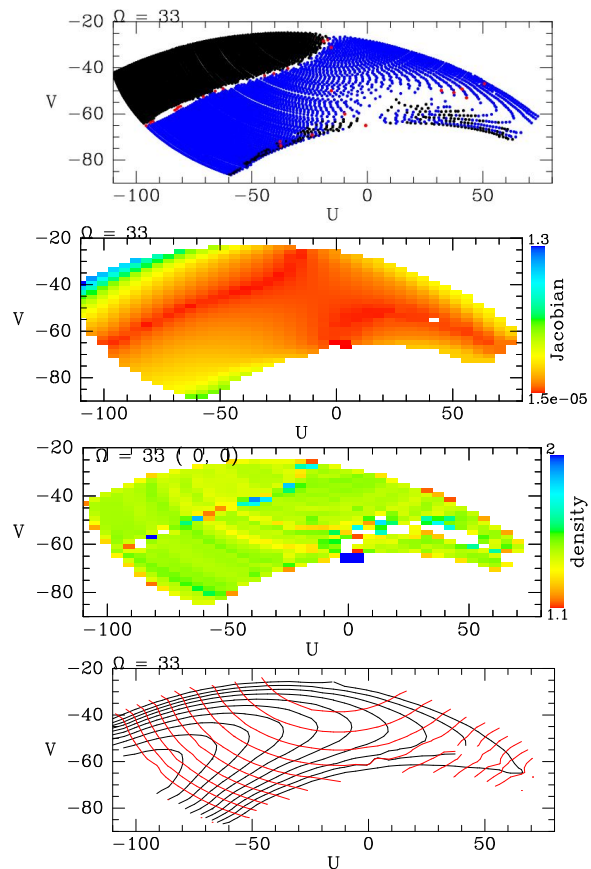


Figure 1. The location in local velocity space of orbits trapped at corotation by a bar with pattern speed $33 \text{ Gyr}^{-1} \simeq 33 \text{ km s}^{-1} \text{ kpc}^{-1}$. The top panel shows the velocities at which trapped orbits pass through the Sun. Most orbits reach us with two velocities (with $v_z > 0$); one velocity is plotted in black and the other in blue. The second panel down shows the value of the Jacobian (1). The third panel down shows (on a logarithmic scale) the (essentially uniform) density in velocity space generated by the way we have sampled action space. The bottom panel shows contours of constant J_r in red and constant \mathcal{J} in black. The range of libration actions is $(0.053, 0.16) \text{ kpc}^2 \text{ Myr}^{-1}$.

on approximate ellipses in the (U, V) plane that have near uniformly spaced semi-axis lengths. The \mathcal{J} coordinate of the n th grid point was

$$\mathcal{J}_n = \mathcal{J}_{\min} + (n/N)^2 [\mathcal{J}_{\max} - \mathcal{J}_{\min}]. \quad (4)$$

Here N is the total number of \mathcal{J} values to be sampled and \mathcal{J}_{\min} is the least libration action required for an orbit of a given value of the fast action $J'_3 = J_r$ to reach the Sun. \mathcal{J}_{\max} is the largest possible value of \mathcal{J} at the given J'_3 value.

The overwhelming majority of the 3611 orbits (tori) plotted in Fig. 1 visit the Sun at two different velocities. In the top panel one velocity is marked by a blue dot and the other is marked by a black dot. 14 orbits visit at a single velocity and 13 visit with three velocities. These velocities are marked by red dots. The remaining 191 orbits visit with four velocities and two of these velocities are plotted in blue and two in black.

3.1 Density of stars in velocity space

The second panel down shows how the Jacobian D (eqn.1) varies over the plane. It ranges over several orders of magnitude. It is smallest where the density of dots in the top panel is lowest, namely where the blocks of blue and black dots meet, and in the middle right of the wing structure. To understand this connection we write

$$\left(\frac{dn}{d^3\mathbf{v}}\right)_{\mathbf{x}} = \frac{dn}{d^3\mathbf{J}} \left(\frac{\partial(\mathbf{J})}{\partial(\mathbf{v})}\right)_{\mathbf{x}} = f(\mathbf{J}) \left(\frac{\partial(\mathbf{x})}{\partial(\boldsymbol{\theta})}\right)_{\mathbf{J}} = Df(\mathbf{J}). \quad (5)$$

Hence when D is small, the density of dots in velocity space will also be small. The third panel down in Fig. 1 shows the density of stars in velocity computed by adding to the grid of cells, via the cloud-in-cell algorithm, an amount $1/D$ times the area $d\mathcal{J}dJ_r$ of the cell in the (\mathcal{J}, J_r) plane that is represented by that orbit. Thus $f(\mathbf{J})$ is being set to a constant and the plotted density is

$$f(\mathbf{J}) = \frac{1}{D} \frac{dn}{d^3\mathbf{v}}, \quad (6)$$

which should be constant. The third panel shows that to a good approximation it is

The attainment of a constant velocity-space density through cancellation of the large variations in D and in the dot density is striking. The physical significance of these variations is that where the dots are sparse in the top panel, $1/D = \partial(\boldsymbol{\theta})/\partial(\mathbf{x})$ is large because a given torus (almost) reaches the Sun for a wide range of angle variables. Hence parts of velocity space coloured red in the second panel of Fig. 1 are populated by large contributions from a small number of tori.

When comparing observations with distributions in velocity space like those of Fig. 1, one has to be mindful that the observed star density is not $dn/d^3\mathbf{v}$ but $f[\mathbf{J}(\mathbf{x}, \mathbf{v})]$ because it is $dn/d^3\mathbf{v}$ weighted by the real-space density of stars $dn/d^3\mathbf{x}$, which tends to infinity when $dn/d^3\mathbf{v}$ tends to zero.

3.2 Contours of constant action

The bottom panel of Fig. 1 shows contours of constant J_r (red) and constant \mathcal{J} (black). J_r increases from top to bottom, and \mathcal{J} increases from left to right along the centre of the wing-shaped region. The two sets of contours become tangent to one another along the curve on which the blocks of black and blue dots meet in the top panel. This parallelism indicates that the matrix $\partial v_i / \partial J_j$ that connects the \mathbf{v} and \mathbf{J} coordinate systems for velocity space has become degenerate. This does not imply any failure of the $(\boldsymbol{\theta}, \mathbf{J})$ system; it just signals that one needs to specify the value of an angle variable in addition to the value of J_r (or \mathcal{J}) to specify unambiguously a velocity. As \mathcal{J} decreases, the black contours shrink onto a point that lies near $(-100, -70) \text{ km s}^{-1}$. This is the velocity of the orbit that has the minimum libration action (~ 0.053) required to reach the Sun: $\mathcal{J} = 0$ for the closed resonant orbit, which does not pass through the Sun.

The red and black contours are also tangent in the lower right of the wing, where the dots are very sparse in the top panel.

Fig. 2 shows how the radial and libration periods $2\pi/\Omega_r$ and $2\pi/\Omega_\ell$ vary within velocity space. The radial periods lie within the very narrow range 130 to 132 Myr while the libration periods, which increase with libration amplitude, are all

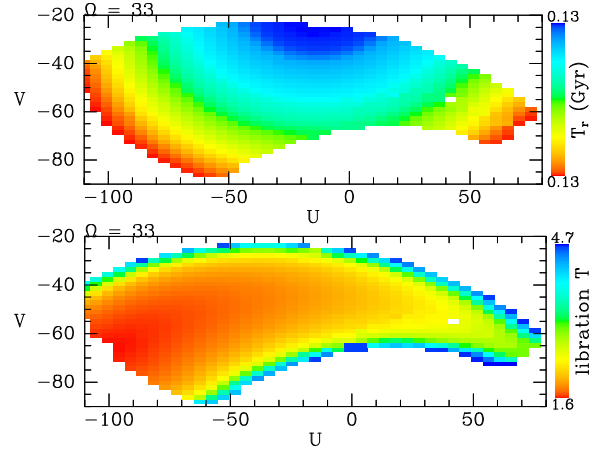


Figure 2. The radial period (upper) and libration period (lower) of orbits trapped at corotation as a function of solar-neighbourhood velocity. Periods are given in Gyr.

longer by more than an order of magnitude. The shortest periods are ~ 1.6 Gyr and the longest plotted exceed 4.6 Gyr. Strictly, the periods go to infinity at the edge of the trapping zone, but the increase with \mathcal{J} is finally very rapid and orbits with very long libration periods are probably unphysical.

3.3 Comparison with Gaia data

The top panel of Fig. 3 superposes the contours of constant action from the bottom panel of Fig. 1 onto a representation of the density of stars in the Gaia catalogue that lie within 0.3 kpc of the Sun and have line-of-sight velocities in the Gaia DR2 catalogue. This representation is designed to bring out local fluctuations in the star density that are easily masked by the large contrast in the stellar density between $(U, V) \simeq (0, 0)$ and the edge. Specifically, the plotted quantity is the logarithm to base 10 of ratio of the measured star density to the density given by an analytic DF for the discs (thin and thick) and the stellar halo.

In Fig. 3 the region covered by the contours is more extensive than the part of the plane that lies below the depression that runs across the figure from centre left to lower right. However, if one trimmed the contours back to include only orbits with libration periods shorter than ~ 2 Gyr, they would fit the region below the depression rather nicely. The middle panel of Fig. 3 superposes contours for $\Omega_p = 36 \text{ Gyr}^{-1}$. The contours now seem unconnected to the data. The bottom panel, which shows contours for $\Omega_p = 38 \text{ Gyr}^{-1}$ reveals an alternative fit to the data: now the contours provide a reasonable fit to a depression in the observed star density that lies below the one that might be fitted by $\Omega_p = 33 \text{ Gyr}^{-1}$.

3.4 Implication of Jeans theorem

In Fig. 3, most contours of constant \mathcal{J} cut several contours of constant J_r twice. Hence we can identify sets of velocities that correspond to identical actions. If Jeans' theorem were to apply, the DF, and therefore the density of stars in the UV plane, would take the same value at every point in a given set of points. We can easily test this conjecture since

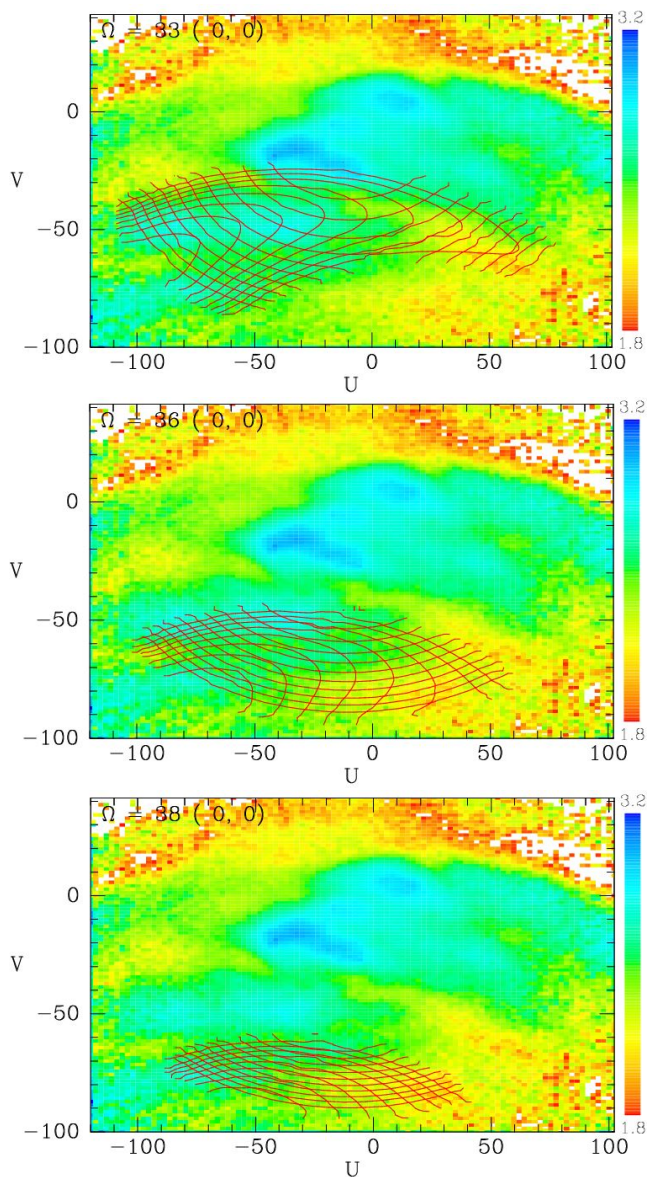


Figure 3. The contours of constant actions for orbits trapped by a bar with pattern speeds 33 (top) 36 (middle) and 38 Gyr^{-1} superposed on the density of stars in velocity space obtained by selecting stars that lie within 0.3 kpc and have line-of-sight velocities from the RVS. The quantity plotted is the logarithm to base 10 of the ratio of the measured density to the prediction of an analytic DF.

our tori visit just such matched points, and at these points we should find equal densities of Gaia stars. Fig. 4 shows the statistic

$$\Delta \equiv \left\langle \frac{\overline{n^2} - \overline{n}^2 - \overline{n}}{\overline{n}^2} \right\rangle. \quad (7)$$

Here n is the number of Gaia stars in the UV bin picked out by a visiting torus and an overline indicates a mean over the points visited by a single torus while the angle brackets indicate a mean over all relevant tori. The first two terms in the fraction's numerator give the variance in the number of stars in the bins visited by a single torus and the third term corrects for the contribution of Poisson noise. If Jeans's the-

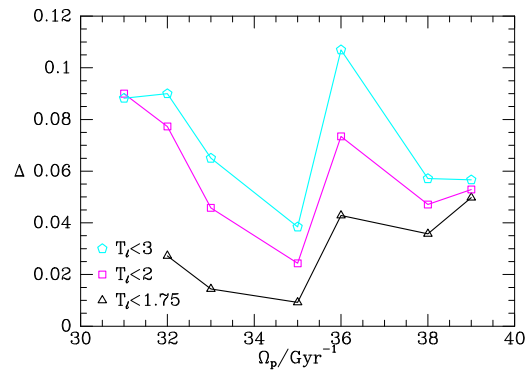


Figure 4. The statistic (7) for different bar pattern speeds and maximum libration periods T_ℓ . Each symbol corresponds to a maximum libration period as marked in Gyr.

orem were perfectly observed, the numerator would average to zero. Three points are shown for each value of Ω_p , being the points obtained by including only tori with libration periods shorter than 1.75, 2 and 3 Gyr on the grounds that Jeans theorem is most likely to apply to the tori with the shortest libration periods. The figure shows that in general longer maximum libration periods yield larger values of Δ as expected, but the scatter this induces does not obscure systematic variation of Δ with Ω_p . For every maximum period Δ takes its minimum value at $\Omega_p = 35 \text{ Gyr}^{-1}$, and the smallest upper limit on T_ℓ favours values in the range 32 – 36 Gyr^{-1} .

4 ORBITS TRAPPED AT OLR

At OLR the slow angle is $\theta'_1 = \theta_r + 2\theta_\phi$. The value of this linear combination of θ_r and θ_ϕ is set by the action of libration θ_ℓ . The fast action is $J'_3 = J_\phi - 2J_r$ and it is complemented by the action of libration \mathcal{J} .

Fig. 5 shows the footprint in the UV plane of orbits that are trapped at the OLR with $\Omega_p = 43 \text{ Gyr}^{-1}$. As in the case of corotation, the great majority of trapped orbits visit the Sun (with $v_z > 0$) at either two or four points in the UV plane: in this case 682/1000 visit twice (blue/black dots) and 220 visit four times (red dots). The middle panel of Fig. 5 explains the increased popularity of four visits: several red contours (of constant $J_\phi - 2J_r$) cut black contours (of constant \mathcal{J}) four times each, whereas in the bottom panel of Fig. 1 each red contour cuts a black contour at most twice. We saw above that orbits correspond to intersections of contours, so four intersections implies four visit. Stars that visit twice have either the smallest J_r or the smallest \mathcal{J} consistent with reaching the Sun.

The bottom panel of Fig. 5 shows that all orbits contributing to Fig. 5 have long libration periods: periods start at 2.2 Gyr.

Fig. 6 overlays contours like those plotted in the middle panel of Fig. 5 on the representation of the density of stars in the Gaia DR2 RVS sample used in Fig. 3. For $\Omega_p \lesssim 37 \text{ Gyr}^{-1}$ the region occupied by trapped orbits lies at values of V that are too large to be of interest. Consequently, if trapping at corotation is relevant, as Fig. 3 suggests, trapping at OLR will be unimportant. In Fig. 6 the region occupied by trapped orbits moves down as Ω_p increases. The upper

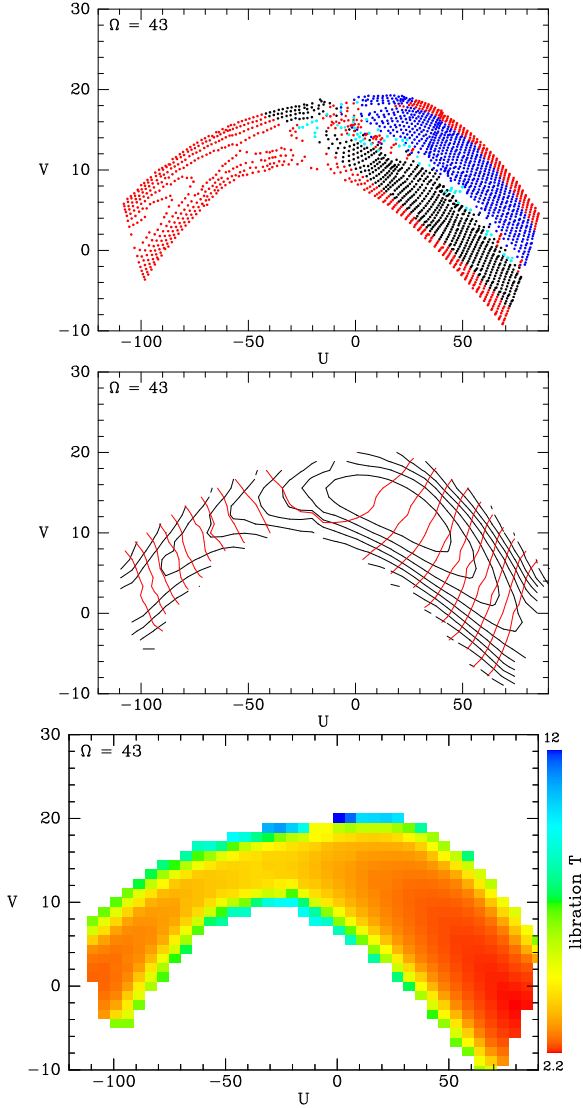


Figure 5. The locations in local velocity space of orbits trapped at OLR of a bar with pattern speed 43 Gyr^{-1} . The top panel shows the velocities at which trapped orbits pass through the Sun. Most orbits reach us with either two (black/blue points) or four (red points) velocities (with $v_z > 0$). Cyan points mark single or triple visits. In the second panel down red curves are contours of the conserved action $J'_3 = J_r - 2J_\phi$ while contours of constant libration action \mathcal{J} are black. The values of \mathcal{J} increase with the length of the contour, while the values of J'_3 increase roughly with $|U|$. The bottom panel shows the means in each cell of the libration period. Note that, unlike in Fig. 1 the vertical and horizontal scales differ.

boundaries of the regions of trapping in the lower two panels of Fig. 6 are occupied by orbits with the largest values of J'_3 and thus the smallest values of J_r . That is, the top edges of these panels lie on contours of constant J'_3 .

The middle panel of Fig. 6 shows that when $\Omega_p = 50 \text{ Gyr}^{-1}$ they reach the Sun with small negative values of V , and for the most part positive values of U . Fig. 7 explains the bias to positive U (movement towards the Galactic Centre) by showing part of an orbit with a small value of \mathcal{J} together with the location of the Sun. In an inertial frame the bar and the disc rotate counter-clockwise, but pictured here in the

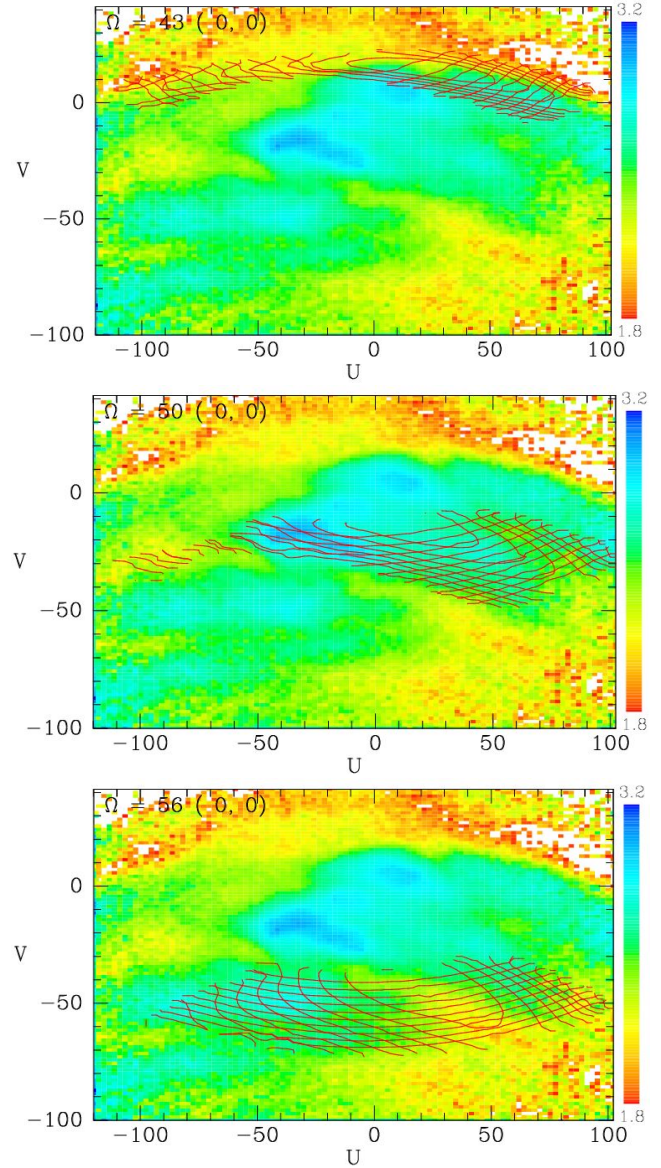


Figure 6. The density of RVS stars in local velocity space as in Fig. 3 together with contours of constant actions for orbits trapped at the OLR of bars with pattern speeds (from top to bottom) $\Omega_p = 38, 50$ and 56 Gyr^{-1} .

bar's frame the orbit circulates clockwise, and as it passes the Sun, it is moving from apocentre at the bar's major axis towards pericentre near the minor axis. Hence orbits with small \mathcal{J} visit us with $U > 0$.

Of the 2139 orbits computed for $\Omega_p = 50 \text{ Gyr}^{-1}$, 1795 visit the Sun twice with $v_z > 0$ and just 246 visit three or four times. Thus increasing Ω_p has made four visits less popular. The stars that still visit four times make up the tail of contours in the middle panel of Fig. 6 that extends leftwards of $U = -60 \text{ km s}^{-1}$. The tail is made up of stars with large libration actions that also visit on the upper and lower edges of the band of contours at $U > 0$ (cf. the top panel of Fig 5).

The bottom panel of Fig. 6 shows that when $\Omega_p = 56 \text{ Gyr}^{-1}$ the region occupied by trapped orbits has moved to lower V than in the middle panel for $\Omega_p = 50 \text{ Gyr}^{-1}$, and

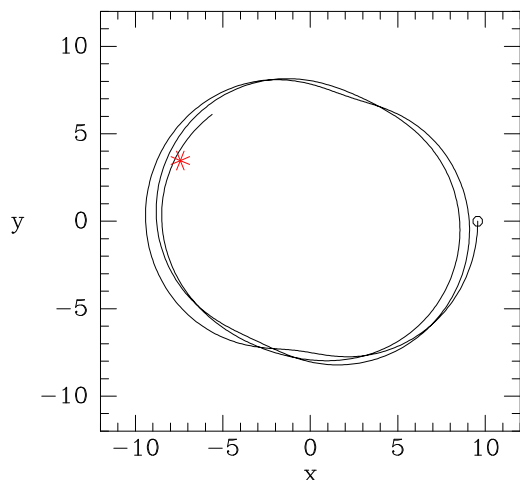


Figure 7. A section of an orbit trapped at OLR in a bar with $\Omega_p = 50 \text{ Gyr}^{-1}$. The circle marks the launch point and the star marks the Sun's location.

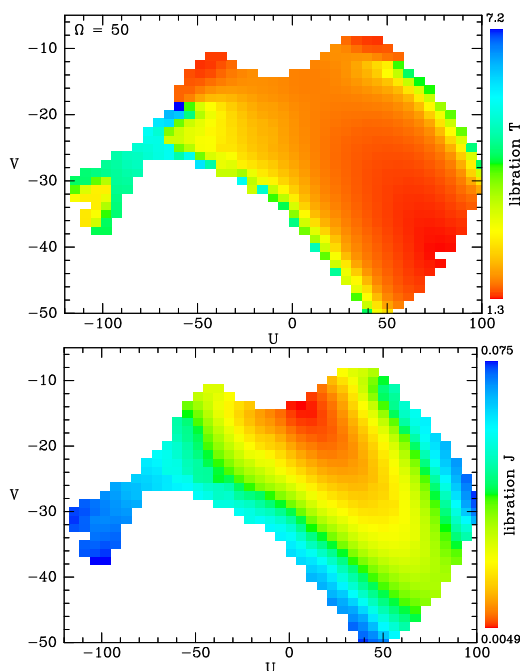


Figure 8. Upper panel: The distribution of libration periods of orbits trapped at OLR when $\Omega_p = 50 \text{ Gyr}^{-1}$. Lower panel: Distribution of libration actions \mathcal{J} of these orbits.

is now less biased to positive U . The tail formed by stars that visit four times has vanished.

Even for large values of Ω_p , orbits trapped at OLR all have very long libration periods: the upper panel of Fig. 8 shows that with $\Omega_p = 50 \text{ Gyr}^{-1}$ the libration periods start at 1.3 Gyr; with $\Omega_p = 56 \text{ Gyr}^{-1}$ they start at 0.92 Gyr. Consequently, there is no compelling case for Jeans' theorem applying to these orbits.

Fig. 9 shows the location in action space of visiting orbits for three values of Ω_p . As the pattern speed increases, the OLR moves in towards the Sun. When the OLR is distant, the Sun can be reached only from eccentric resonant orbits, and then only with a large libration amplitude. As

the OLR approaches, smaller libration amplitudes are required to reach the Sun, and it becomes easier to reach the Sun from the least eccentric resonant orbit. Consequently, the block of orbits that visit us moves down and to the left in Fig. 9. In the right two panels, the spikes at $J_r \simeq 0.02$ along the top edges of the populated region signal the value of J_r at which a clear division between trapped and untrapped orbits vanishes, as explained in the companion paper.

In Fig. 6 the only intriguing coincidence between a feature in the observed star density and the structure of a trapped zone is the match in the middle panel between the most pronounced ridge in the star density and the lower edge of the zone. However, the statistic Δ defined by equation (7) indicates that the broader structure of the zone is incompatible with the hypothesis that the DF is a function of the resonant actions: $\Delta = 0.51$ when orbits with libration periods $T_\ell < 5 \text{ Gyr}$ are included and 0.50 when only orbits with $T_\ell < 3 \text{ Gyr}$ are included. For comparison, the top and bottom panels yield $\Delta = 0.64, 0.37$ for $T < 5 \text{ Gyr}$ and 0.48, 0.37 for $T < 3 \text{ Gyr}$. Not only are all these values significantly larger than the values plotted in Fig. 4 for the case of trapping at corotation, but inspection of the middle panel of Fig. 6 makes clear why Δ is so large in the case $\Omega_p = 50 \text{ Gyr}^{-1}$: intersections of contours in the heavily populated, deep blue region $(-30, -18) \text{ km s}^{-1}$ are paired with intersections of the same contours in the much more sparsely populated light blue region around $(58, -16) \text{ km s}^{-1}$.

5 VELOCITY SPACES A KPC AWAY

Gaia, unlike Hipparcos, allows us to examine velocity space at locations that are significantly removed from the Sun. Fig. 10 shows the star densities at the four locations reached by moving 1 kpc towards or away from the Galactic centre and in or against the direction of Galactic rotation. In each case stars are included if they lie within 0.3 kpc of the point in question. The contours overplotted are those of constant actions for trapping at corotation with $\Omega_p = 33 \text{ Gyr}^{-1}$. In these panels the coordinate system is strictly Cartesian, so U is the component of velocity that is towards the Galactic centre at the Sun, but not at the locations $(0, \pm 1)$ plotted to left and right of the centre panel. The distribution of stars is centred on negative U at $(x, y) = (0, -1)$ and on positive U at $(0, 1)$ because at these locations the circular velocity has a non-vanishing U component with that sign.

Fig. 10 shows that zones of entrapment move around velocity space quite rapidly as we move around the Sun. While no striking agreement between star densities and zones of entrapment is evident, it is in every panel possible to imagine qualitative similarities. The statistic Δ defined by equation (7) is negative ($-0.38, -0.33$ and -0.085) for three locations ($x = \pm 1$ and $y = 1$), indicating that deviations from the predictions of Jeans' theorem are smaller than are expected from Poisson noise. By contrast, $\Delta = 0.24$ at $y = -1$. This positive value may be no more than a random upwards fluctuation, but it may reflect a tendency for velocities $(U, V) \simeq (-20, -65) \text{ km s}^{-1}$ with low densities to be matched with $(-70, -45)$ where the density is much higher.

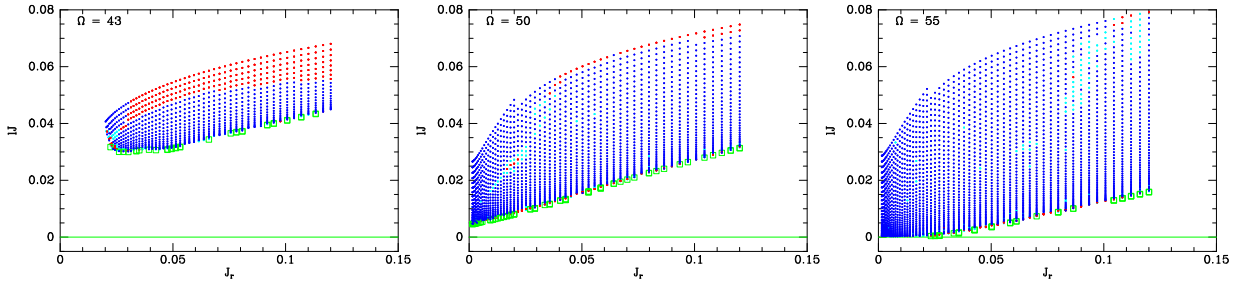


Figure 9. Locations in action space of orbits trapped at OLR that visit the Sun. On the x axis we have the radial action of the underlying perfectly resonant orbit: the conserved action J'_3 is a function of this value. Libration actions \mathcal{J} are plotted vertically. A blue point indicates two visits to the Sun with $v_z > 0$, a red point indicates four such visits, and a cyan point indicates one or three visits. A green square indicates a failure to visit.

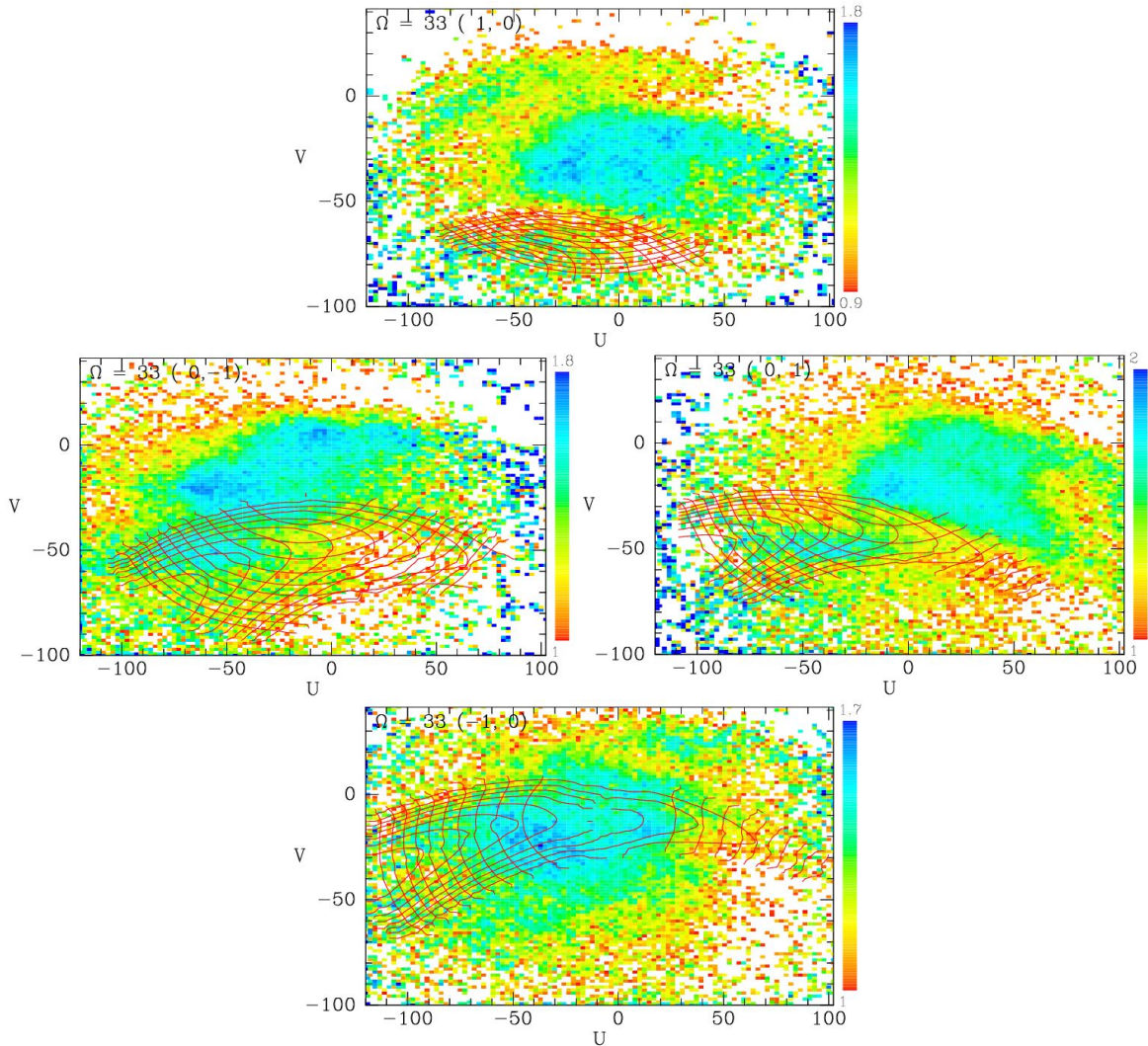


Figure 10. Contours of constant actions when $\Omega_p = 33 \text{ Gyr}^{-1}$ superposed on the density of RVS stars in the velocity space at four locations 1 kpc from the Sun. The anticentre lies upwards and rotation takes stars from left to right.

6 CONCLUSIONS

An improved version of the torus-mapping code TM has been used to determine the velocity-space locations of stars that are trapped at the corotation and outer Lindblad resonances of bars of various pattern speeds. TM computes the actions

of trapped stars so one can add to the observed density of stars in velocity space contours of the two functions on which the Galaxy's DF would depend if Jeans' theorem applied to trapped orbits. From intersections of contours one can identify sets of two, three or four velocities at which the density of stars would be equal if the adopted potential were

correct and Jeans' theorem applied. Equation (7) defines a measure Δ of the extent to which the observed star density violates this prediction. A plot of Δ versus pattern speed weakly supports trapping at corotation in a bar with pattern speed $(34 \pm 2) \text{ Gyr}^{-1}$. The values taken by Δ at locations displaced from the Sun by a kpc in the cardinal directions are consistent with the hypothesis of trapping at corotation with $\Omega_p = 33 \text{ Gyr}^{-1}$.

The above chain of argument is open to the objection that the libration periods of trapped orbits may be too long for Jeans' theorem to apply because stars have not had time to phase mix. At corotation libration periods tend to be $\gtrsim 1.6 \text{ Gyr}$ and larger than the radial period by a factor ~ 12 . An indication that this issue is a real one is the tendency of Δ for increase as tori with longer libration periods are included.

The Δ statistic offers no support for the hypothesis that trapping at the OLR is important. A fundamental problem with a connection between the Hercules stream and trapping at the OLR is that stars trapped in a fast bar tend to visit the Sun at $U > 0$ (approaching the Galactic centre) whereas the Hercules stream lies at $U < 0$. The libration periods of stars trapped at the OLR of a fast bar are only slightly shorter than the libration periods of stars trapped at corotation when $\Omega_p \simeq 33 \text{ Gyr}^{-1}$.

The impact of resonant trapping on Gaia data has two distinct aspects. One is the nature of trapped orbits, which has been addressed here. Another is how those orbits are populated, which is a much harder question. From Dehnen's seminal (1999) study onwards most analyses of velocity space have implicitly assumed that the density of stars can be predicted by assuming adiabatic growth of the bar's strength at a constant pattern speed. There is no physical basis for this assumption and the question of how trapped orbits are populated cannot be answered so simply.

The bar is unlikely to have a constant pattern speed because the latter is a measure of the angular momentum in the bar, which has both sources and sinks. Dynamical friction of the bar against the dark halo and the outer disc removes angular momentum, making the bar slower and longer. Conversely, angular momentum is stripped from gas that falls through corotation and is then funnelled to the central molecular zone (Debattista & Sellwood 2000; Athanassoula 2002, 2003). N-body simulations suggest that the bar gradually slows, so its resonances move out through the disc.

A star whose orbit lies in the path in action space of a resonance has a probability to become trapped (and hence transferred to the action space of trapped orbits), and a probability to be dumped on the far side of the resonance. The magnitudes of these probabilities depend on the speed at which the resonance is moving and growing/shrinking. Indeed, if the resonance is shrinking, stars will always be dumped, while if it is growing strongly while moving slowly, a star is much more likely to be trapped than dumped. These considerations imply that the DF within a trapped zone will depend on the complete history of the relevant resonance and thus of the bar.

Some stars will have become trapped during bar formation, which happens essentially on a dynamical timescale (Raha et al. 1991). Such stars may have been transported a significant distance outwards. Other stars will have been swept up later as the bar slowed and strengthened. Hence

the density of stars in and around a bar's trapped zone in velocity space must contain a wealth of information about the history of our disc.

The natural approach is to follow the dynamics of stars using the angle-action coordinates of the instantaneous bar. Chiba et al. (2020) have recently made a start on this enterprise in the context of a simple razor-thin disc. The task is challenging because both the instantaneous bar structure and its history have to be inferred. The technology displayed here could be used to develop this line of attack. In this context the ability of TM to model vertical motions in parallel with motion in the plane is likely to prove important because J_z is known to be strongly correlated with chemistry and age (e.g. Bland-Hawthorn et al. 2019).

Monari et al. (2019) have recently presented evidence that some of the ridges in the Gaia DR2 data evident in Figs. 3 and 6 are associated with resonances driven by $m = 3$ and $m = 4$ components of the bar's potential. It would be straightforward to apply TM to these resonances.

ACKNOWLEDGEMENTS

This work has been supported by the Leverhulme Trust and the UK Science and Technology Facilities Council under grant number ST/N000919/1.

REFERENCES

- Athanassoula E., 2002, *ApJ*, 569, L83
- Athanassoula E., 2003, *MNRAS*, 341, 1179
- Binney J., 2012, *MNRAS*, 426, 1324
- Binney J., 2016, *MNRAS*, 462, 2792
- Binney J., 2018, *MNRAS*, 474, 2706
- Binney J., 2020, *MNRAS*, submitted
- Binney J., Kumar S., 1993, *MNRAS*, 261, 584
- Binney J., McMillan P. J., 2016, *MNRAS*, 456, 1982
- Binney J., Schönrich R., 2018, *MNRAS*, 481, 1501
- Bland-Hawthorn J., Sharma S., Tepper-García T., Binney J., Freeman K. C., Hayden M. R., Kos J., De Silva G. M., Ellis S., Lewis G. F., Asplund M., Buder S., 2019, *MNRAS*, 486, 1167
- Casagrande L., Schönrich R., Asplund M., Cassisi S., Ramírez I., Meléndez J., Bensby T., Feltzing S., 2011, *A&A*, 530, A138
- Chiba R., Friske J. K. S., Schönrich R., 2020, *MNRAS*, submitted
- De Simone R., Wu X., Tremaine S., 2004, *MNRAS*, 350, 627
- Debattista V. P., Sellwood J. A., 2000, *ApJ*, 543, 704
- Dehnen W., 1998, *AJ*, 115, 2384
- Dehnen W., 1999, *ApJL*, 524, L35
- Dehnen W., 2000, *AJ*, 119, 800
- Famaey B., Jorissen A., Luri X., Mayor M., Udry S., Dejonghe H., Turon C., 2005, *A&A*, 430, 165
- Fragkoudi F., Katz D., Trick W., White S. D. M., Di Matteo P., Sormani M. C., Khoperskov S., Haywood M., Hallé A., Gómez A., 2019, *MNRAS*, 488, 3324
- Gaia Collaboration Brown A. G. A. e. a., 2018, *A&A*, 616, A1
- Gaia Collaboration Katz D. e. a., 2018, *A&A*, 616, A11

- Hahn C. H., Sellwood J. A., Pryor C., 2011, MNRAS, 418, 2459
- Holmberg J., Nordström B., Andersen J., 2009, A&A, 501, 941
- Hunt J. A. S., Bub M. W., Bovy J., Mackereth J. T., Trick W. H., Kawata D., 2019, MNRAS, 490, 1026
- Jeans J. H., 1916, MNRAS, 76, 567
- Kaasalainen M., 1994, MNRAS, 268, 1041
- Kaasalainen M., 1995a, MNRAS, 275, 162
- Kaasalainen M., 1995b, Phys. Rev. E, 52, 1193
- Kaasalainen M., Binney J., 1994, MNRAS, 268, 1033
- McGill C., Binney J., 1990, MNRAS, 244, 634
- McMillan P. J., 2011, MNRAS, 418, 1565
- McMillan P. J., 2013, MNRAS, 430, 3276
- McMillan P. J., 2017, MNRAS, 465, 76
- Monari G., Famaey B., Fouvy J.-B., Binney J., 2017, MNRAS, 471, 4314
- Monari G., Famaey B., Siebert A., Wegg C., Gerhard O., 2019, A&A, 626, A41
- Monari G., Kawata D., Hunt J. A. S., Famaey B., 2017, MNRAS, 466, L113
- Nordström B., Mayor M., Andersen J., Holmberg J., Pont F., Jørgensen B. R., Olsen E. H., Udry S., Mowlavi N., 2004, A&A, 418, 989
- Pérez-Villegas A., Portail M., Wegg C., Gerhard O., 2017, ArXiv e-prints
- Perryman M. A. C., Lindegren L., Kovalevsky J., Hog E., Bastian U., Bernacca P. L., Creze M., Donati F., Grenon M., Grewing M., van Leeuwen F., van der Marel H., Mignard F., 1997, A&A, 500, 501
- Raha N., Sellwood J. A., James R. A., Kahn F. D., 1991, Nat, 352, 411
- Schönrich R., McMillan P., Eyer L., 2019, MNRAS, 487, 3568
- Sellwood J. A., 2010, MNRAS, 409, 145
- Sormani M. C., Binney J., Magorrian J., 2015, MNRAS, 454, 1818
- Trick W. H., Coronado J., Rix H.-W., 2019, MNRAS, 484, 3291
- Trick W. H., Fragkoudi F., Hunt J. A. S., Mackereth J. T., White S. D. M., 2019, arXiv e-prints, p. arXiv:1906.04786
- Vasiliev E., 2019, arXiv e-prints, p. arXiv:1908.00009